

# 1 Detecting m6A RNA modification from nanopore sequencing using a 2 semi-supervised learning framework

3 Haotian Teng<sup>1</sup>[0000-0003-0337-8722], Marcus Stoiber<sup>2</sup>[0000-0000-0000-0000],

4 Ziv Bar-Joseph<sup>1</sup>[0000-0003-3430-6051], and Carl Kingsford<sup>1</sup>[0000-0002-0118-5516]

5 <sup>1</sup> Ray and Stephanie Lane Computational Biology Department, Carnegie Mellon University, Pittsburgh PA 15213, USA  
6 [haotiant@cs.cmu.edu](mailto:haotiant@cs.cmu.edu), [zivbj@cs.cmu.edu](mailto:zivbj@cs.cmu.edu), [carlk@cs.cmu.edu](mailto:carlk@cs.cmu.edu)

7 <sup>2</sup> Oxford Nanopore Technologies

8 [Marcus.Stoiber@nanoporetech.com](mailto:Marcus.Stoiber@nanoporetech.com)

9 **Abstract.** Direct nanopore-based RNA sequencing can be used to detect post-transcriptional base mod-  
10 ifications, such as m6A methylation, based on the electric current signals produced by the distinct chem-  
11 ical structures of modified bases. A key challenge is the scarcity of adequate training data with known  
12 methylation modifications. We present Xron, a hybrid encoder-decoder framework that delivers a direct  
13 methylation-distinguishing basecaller by training on synthetic RNA data and immunoprecipitation-based  
14 experimental data in two steps. First, we generate data with more diverse modification combinations  
15 through in silico cross-linking. Second, we use this dataset to train an end-to-end neural network base-  
16 caller followed by fine-tuning on immunoprecipitation-based experimental data with label-smoothing. The  
17 trained neural network basecaller outperforms existing methylation detection methods on both read-level  
18 and site-level prediction scores. Xron is a standalone, end-to-end m6A-distinguishing basecaller capa-  
19 ble of detecting methylated bases directly from raw sequencing signals, enabling de novo methylome  
20 assembly.

21 **Keywords:** Nanopore sequencing · m6A RNA modification · Deep learning · hidden Markov model.

## 22 Introduction

23 RNA modification plays essential roles in various biological processes, including stem cell differentiation and  
24 renewal, brain functions, immunity, aging, and cancer progression (Boulias & Greer 2023; Sun et al. 2019;  
25 D'Aquila et al. 2017; Qin et al. 2020). Among the various types of RNA modifications, N6-Methyladenosine  
26 (m6A) is one of the most abundant versions and is involved in various biological processes including mRNA  
27 expression, splicing, nuclear exporting, translation efficiency, RNA stability, and miRNA processing (Boulias

28 & Greer 2023). Accurate detection and quantification of m6A modifications is crucial for understanding their  
29 impact on gene regulation and cellular processes (Murakami & Jaffrey 2022; Fu et al. 2014).

30 High-throughput sequencing from Illumina, also known as sequencing by synthesis (SBS), identifies nu-  
31 cleotides through synthesis, leading to the loss of post-transcriptional information (Buermans & Den Dunnen  
32 2014). Therefore, indirect methods are required to detect RNA modifications with SBS. These approaches  
33 first isolate the modified RNA and then conduct reverse transcription and cDNA sequencing to reveal the  
34 modifications. Two primary strategies are used to experimentally isolate RNA modifications. One type of ap-  
35 proach involves immunoprecipitation. Examples of methods using this approach include MeRIP-Seq (Meyer  
36 et al. 2012), m6A-Seq (Dominissini et al. 2012), PA-m6A-Seq (Chen et al. 2015), m6A-CLIP/IP (Ke et al.  
37 2015), miCLIP (Linder et al. 2015), m6A-LAIC-Seq (Molinie et al. 2016), m6ACE-seq (Koh et al. 2019),  
38 and m6A-Seq2 (Dierks et al. 2021). These methods rely on antibodies that target the modified ribonu-  
39 cleotide and enrich the RNA fragments with the target modified bases. The other type of approach is  
40 chemical-based detection. Examples of methods using this approach are Pseudo-Seq (Carlile et al. 2014),  
41 AlkAniline-Seq (Marchand et al. 2018), Mazter-Seq (Garcia-Campos et al. 2019), m6A-REF-Seq (Zhang et  
42 al. 2019), DART-Seq (Meyer 2019), RBS-Seq (Khoddami et al. 2019), and m6A-SAC-seq (Hu et al. 2022).  
43 These techniques use chemical compounds or enzymes that selectively interact with the modified ribonu-  
44 cleotide, either cleaving or modifying the RNA reads to halt or disturb the reverse transcription process.  
45 This is followed by short-read cDNA sequencing, which identifies the RNA modifications by comparing the  
46 read ends of the cDNA or the base mismatches/deletions in cDNA. Although these methods were able to  
47 generate detailed maps of RNA modification sites, they all use external compounds which makes it hard to  
48 obtain the required single base resolution. They also face other challenges and shortcomings including the  
49 limited availability of antibodies or compounds for specific modifications (Ryvkin et al. 2013), nonspecific  
50 antibody binding (Helm et al. 2019; McIntyre et al. 2020; Zhang et al. 2021), low single-nucleotide resolu-  
51 tions (Meyer et al. 2012; Dominissini et al. 2012), and, importantly, an inability to identify the exact location  
52 of a modification.

53 Direct RNA sequencing using nanopores offers a promising alternative (Garalde et al. 2018). An RNA  
54 molecule can be sequenced by measuring the intensity of the current flowing through the pore as the RNA  
55 molecules pass through it. Modified RNA nucleotides produce different signals than their unmodified coun-  
56 terparts, providing information about the modifications at the single-molecule read resolution (Jenjaroen-  
57 pun et al. 2021; Leger et al. 2021). However, to detect specific modifications from subtle signal changes

58 we need an optimized algorithm, which is normally obtained through supervised learning or a comparative  
59 approach (Wan et al. 2022). Unfortunately, current data are not immediately suitable for supervised learning  
60 due to the lack of experimental techniques for identifying the methylation state at the single-read resolution.

61 *In vitro* transcription (IVT) data, which are transcribed from either experimentally synthesized DNA se-  
62 quences or native DNA (Liu et al. 2019; Jenjaroenpun et al. 2021), can provide reads that are either  
63 completely methylated or not methylated at all (all-or-none). However, the diversity of the sequence com-  
64 positions in synthesized DNA datasets is limited due to constraints concerning the maximum DNA length  
65 that can be synthesized and the associated costs. In addition, the IVT dataset lacks partially methylated  
66 reads with known methylation states. Although partially methylated reads can be generated by introducing  
67 a mixture of modified and canonical adenine during *in vitro* transcription, the location of methylation remains  
68 unknown because in such mixtures the RNA polymerase randomly selects adenine from either type during  
69 the transcription process. Models trained to identify modifications on all-or-none modified reads perform  
70 poorly on biological reads, which are usually sparsely methylated, regardless of the training feature used,  
71 such as basecalling error or signal difference (Liu et al. 2019; Zhong et al. 2023). Methods using such  
72 synthesized datasets include training a classifier to predict sequence segments (5-mers) given their corre-  
73 sponding nanopore raw signal segments (Gao et al. 2021) or features of these segments (Liu et al. 2019;  
74 Jenjaroenpun et al. 2021; Leger et al. 2021; Pratanwanich et al. 2021). The signal segments are extracted  
75 from raw signal after performing base-calling and alignment, using models trained on canonical data (data  
76 with no methylation). As we show, the performance of such a classifier is limited since it is only trained  
77 on isolated short segments, losing contextual information. In addition, these models are trained solely on  
78 manually selected features including mean, standard deviation, and duration of isolated signal segments  
79 corresponding to 5 bases, which can lead to the loss of more detailed signal information. Recently, a new  
80 method, CHEUI, was trained using longer signal segments, yielding impressive results on IVT data (Mateos  
81 et al. 2022). However, it suffers from overfitting when applied to real biological samples (Fig. 2, Hendra et al.  
82 (2022)).

83 Immunoprecipitation (IP) data from assays such as m6ACE-seq and m6A-CLIP-seq relies on the use of an-  
84 tibodies (Linder et al. 2015; Ke et al. 2015; Schwartz et al. 2013). However, this strategy only provides the  
85 modification proportion for each reference transcriptomic position, i.e., a site-level modification rather than  
86 the modification state for each individual read (read-level). m6Anet (Hendra et al. 2022) employs multiple-  
87 instance learning (Amores 2013) to train a classifier using IP data leading to improved site-level accu-

88 racy. However, IP data misses many methylation sites, particularly in low-coverage regions (McIntyre et al.  
89 2020). Additionally, due to nonspecific antibody binding, the methylation detection results obtained through  
90 immunoprecipitation experiments produced a false-positive rate of approximately 11%, which can vary be-  
91 tween studies (Ke et al. 2017; Garcia-Campos et al. 2019). M6Anet also requires a minimum coverage level  
92 of 20 reads for a site to be detected due to the way the model is trained. The training involves maximizing  
93 the probability of detecting at least one methylated read among the reads covering a known methylated site.  
94 Such coverage depth is not always available. Finally, as in the other existing models, m6Anet relies on a  
95 basecaller and segmentation tools that are trained on nonmodified reads (canonical reads).

96 In summary, previous approaches try to identify m6A sites using basecalling errors (Liu et al. 2019; Jen-  
97 jaroenpun et al. 2021; Leger et al. 2021; Pratanwanich et al. 2021), by comparing between control sam-  
98 ples (Leger et al. 2021; Abebe et al. 2022), trained on IVT data (Gao et al. 2021; Mateos et al. 2022) or  
99 trained on noisy labels from IP data (Hendra et al. 2022). As we will show, the fact that they are only trained  
100 on one type of data limits their performance. This work aims to address these limitations by introducing  
101 a framework that integrates multiple data types to improve the identification of m6A sites in direct RNA  
102 Nanopore sequencing.

## 103 Results

104 We present a method that takes a different approach by detecting methylation during the basecalling phase.  
105 We predict methylated bases directly from the current signal by training a methylation-distinguishing base-  
106 caller. To achieve this, we developed Xron, a hybrid encoder-decoder framework (Fig. 1). The encoder is a  
107 convolutional recurrent neural network (CRNN) encoding the observable signal into a  $k$ -mer representation.  
108 After it has been trained and fine-tuned, the CRNN serves as a methylation-distinguishing basecaller for  
109 new data. The decoder is a nonhomogeneous hidden Markov model (NHMM), which serves as a gener-  
110 ative model for achieving signal segmentation and alignment when preparing the training dataset. Apply-  
111 ing the NHMM, we created a partially methylated dataset to train the CRNN and produce a methylation-  
112 distinguishing basecaller. The CRNN is then fine-tuned using IP data, further enhancing the basecaller's  
113 generalizability (Supplementary Fig. S2). This framework enables us to obtain a highly accurate methylation-  
114 distinguishing basecaller by exploiting both IVT data and IP data, rather than using just one type of data  
115 (Table S1). This approach outperforms all previous methods on synthesized and biological samples and

116 provides a comprehensive, end-to-end solution for methylation base detection (Table 1, Fig. 2A,B and Sup-  
 117 plementary Fig. S4).

**Table 1.** Reported Performance of m6A Modification Identification Achieved by Existing Works

Method	AUC ROC			
	*Read-level	*Site-level	Yeast KO <sup>1</sup>	Human <sup>2</sup>
Epinano (2019) (Liu et al. 2019)	–	0.90	0.680	–
ELIGOS (2021) (Jenjaroenpun et al. 2021)	–	0.756	0.287 (F1)	–
Nanocompose (2021) (Leger et al. 2021)	–	–	0.18 (F1)	–
nanom6A (2021) (Gao et al. 2021)	–	0.97	0.71	–
CHEUI (2022) (Mateos et al. 2022)	0.806	0.92	–	–
m6Ane (2022) (Hendra et al. 2022)	0.90	0.94	–	0.83
Xron (this work)	<b>0.93</b>	<b>&gt;0.99</b>	<b>0.90</b>	<b>0.91</b>

\*These results were reported on the IVT dataset (Liu et al. 2019), in which single-read m6A modifications were known.

<sup>1</sup>Yeast *ime4Δ* knockout dataset from Liu et al. (2019)

<sup>2</sup>Human HEK293T cell dataset from Chen et al. 2021

## 118 Applying Xron to identify m6A methylation on direct RNA sequencing datasets

119 Xron performs methylation-distinguishing basecalling, outputting methylated bases directly from the raw  
 120 sequencing signal emitted from the nanopore. Its neural network basecaller is trained on an augmented  
 121 partially methylated dataset and then fine-tuned using IP data. We tested Xron on three public direct RNA  
 122 sequencing datasets: an IVT dataset (Liu et al. 2019), a yeast dataset (Liu et al. 2019), and a human  
 123 embryonic kidney cells (HEK293T) dataset (Hendra et al. 2022).

124 The IVT dataset (Liu et al. 2019) was synthesized from artificially designed sequences followed by *in*  
 125 *vitro* transcription. The dataset contains either fully methylated or fully unmethylated reads. Signal intensity  
 126 shows differences around the center base of the *k*-mer between modified and unmodified sites (Fig. 3A and  
 127 Supplementary Fig. S1). The sequences are designed to contain all 5-mers, including the most common  
 128 *k*-mer (GGACT) and all 18 DRACH motifs (Fig. 3A,B).

129 The yeast dataset (Liu et al. 2019) contains direct RNA sequencing reads from two strains, a wild-type strain,  
 130 and a “*ime4Δ*” knockout strain, in which *IME4* was deleted. The deletion of *IME4* results in the complete  
 131 elimination of m6A bases, making it a negative control. The yeast dataset contains three independent  
 132 biological replicates for each strain. Two were used in this study; the first replicate was used for training,  
 133 and the second was used for evaluation.

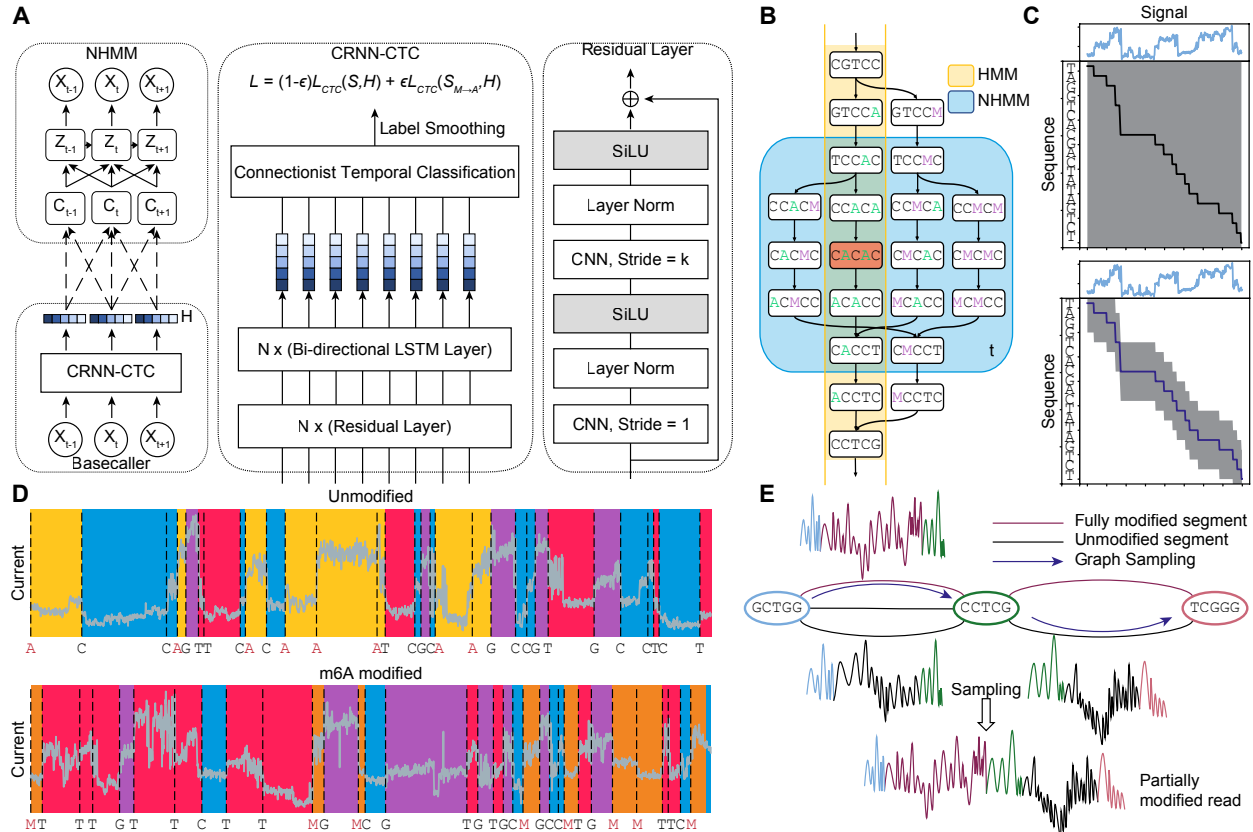


**Fig. 1. Schematics of Xron model and the data augmentation process through crosslinking and sampling.** (A) Xron consists of two parts: a nonhomogeneous hidden Markov model (NHMM) and a convolutional recurrent neural network (CRNN) with a connectionist temporal classification (CTC) decoder. (B) Comparison between HMM and NHMM. The transition matrix of a HMM (yellow) encodes the whole Markov chain of  $k$ -mers, while the transition matrix of the NHMM (blue) at time  $t$  only encodes the Markov chain of the five nearby  $k$ -mers given the predicted  $k$ -mer (shown in red) at time  $t$ . The Markov chain is also expanded to include the  $k$ -mers with all combinations of the A and M (m6A) bases. We create partially methylated reads using data augmentation, first segmenting the signal and then cross-linking the reads and their corresponding signal in silico. To achieve this, we design a novel nonhomogeneous hidden Markov model (NHMM) that can be trained to conduct signal segmentation in a semi-supervised fashion on modified reads, even when lacking methylation labels. The NHMM is trained using the forward-backward algorithm with its transition matrix conditioned on a canonical basecalled sequence and its alignment, thus giving the maximum likelihood estimation of the model parameters regarding methylation base. The Viterbi path of the NHMM gives the alignment between the current signal and sequence. Following the signal segmentation process performed with the NHMM, the NHMM was used to create a training dataset with partially methylated reads and their true labels for methylation detection training by augmenting all-or-none modified reads. (C) The transition process of the NHMM is constrained by the neural network's output, leading to a smaller probability space and making it easier for the model to find the optimal alignment. (D) The NHMM is trained in a semi-supervised manner on IVT datasets, including fully modified, unmodified, and partially modified reads. It provides accurate signal segmentation results for both unmodified and modified sequences. (E) In-silico read crosslinking. The fully modified or unmodified reads are first broken into segments at the invariant  $k$ -mers to form a signal- $k$ -mer graph, whose nodes are  $k$ -mers and whose edges are signal segments. Then, a partially methylated read is sampled from the  $k$ -mer signal graph.

134 The human HEK293T cell dataset (Hendra et al. 2022) contains direct RNA-seq data from the HEK293T  
135 cell line (Pratanwanich et al. 2021), with methylation sites identified by m6ACE-seq (Koh et al. 2019) and  
136 miCLIP data (Linder et al. 2015) on the same cell line. The dataset contains three replicates, and we used  
137 the first replicate to evaluate the method. (See Methods for details about replicates and datasets used for  
138 training and evaluation.)

139 The *Arabidopsis* dataset (Parker et al. 2020) contains direct RNA sequencing reads from wild-type *Ara-*  
140 *bidopsis* (Col-0), mutants (*vir-1*) defective in m6A writer, and VIR-complemented lines. We used the three  
141 replicates of the wild-type line to evaluate the method.

#### 142 **Xron accurately identifies m6A sites**

143 To evaluate the performance of Xron, we applied Xron that is finetuned on yeast data to direct RNA se-  
144 quencing data derived from the human HEK293T cell line (Pratanwanich et al. 2021). Although Xron is  
145 pre-trained using human IVT reads (Methods), no human methylation information is used during training  
146 since all human reads are canonical. To validate the model, we used the m6A sites detected by m6ACE-  
147 seq and miCLIP from the human HEK293T cell line as the true labels during evaluation, following previous  
148 work (Hendra et al. 2022). We used the m6A sites identified by m6ACE-seq and miCLIP as positive sam-  
149 ples and the other sites with the same 5-mer as negative samples. Xron achieved the best ROC AUC of  
150 0.91 (Fig. 2A and Supplementary Fig. S5A) compared with those of Epinano (0.69) and m6Anet (0.83) and  
151 the best precision-recall (PR) AUC of 0.456 (Fig. 2A and Supplementary Fig. S5B) compared to m6Anet  
152 (0.342) and MINES (0.256).

#### 153 **Xron is sensitive to *IME4* knockouts**

154 In addition, we also evaluated Xron on a yeast dataset using a *ime4Δ* knockout *S. cerevisiae* strain where  
155 the m6A modification was completely eliminated (Schwartz et al. 2013) as the control dataset, following a  
156 previous study (Liu et al. 2019). We used the second replicate sample of the dataset for evaluation, as we  
157 had fine-tuned Xron on a subset of the first replicate. We treated the m6A sites in the wild-type strain as  
158 modified sites and the same sites in the *ime4Δ* knockout strain as unmodified sites. We compared Xron with  
159 other models for predicting modified/unmodified sites. Xron achieved an AUC-ROC score of 0.90 (Fig. 2B)  
160 on this task, providing a 21% increase over the second-best model, Epinano (0.72). To fairly compare with  
161 other models that may not have been exposed to the yeast dataset, we evaluated the performance of

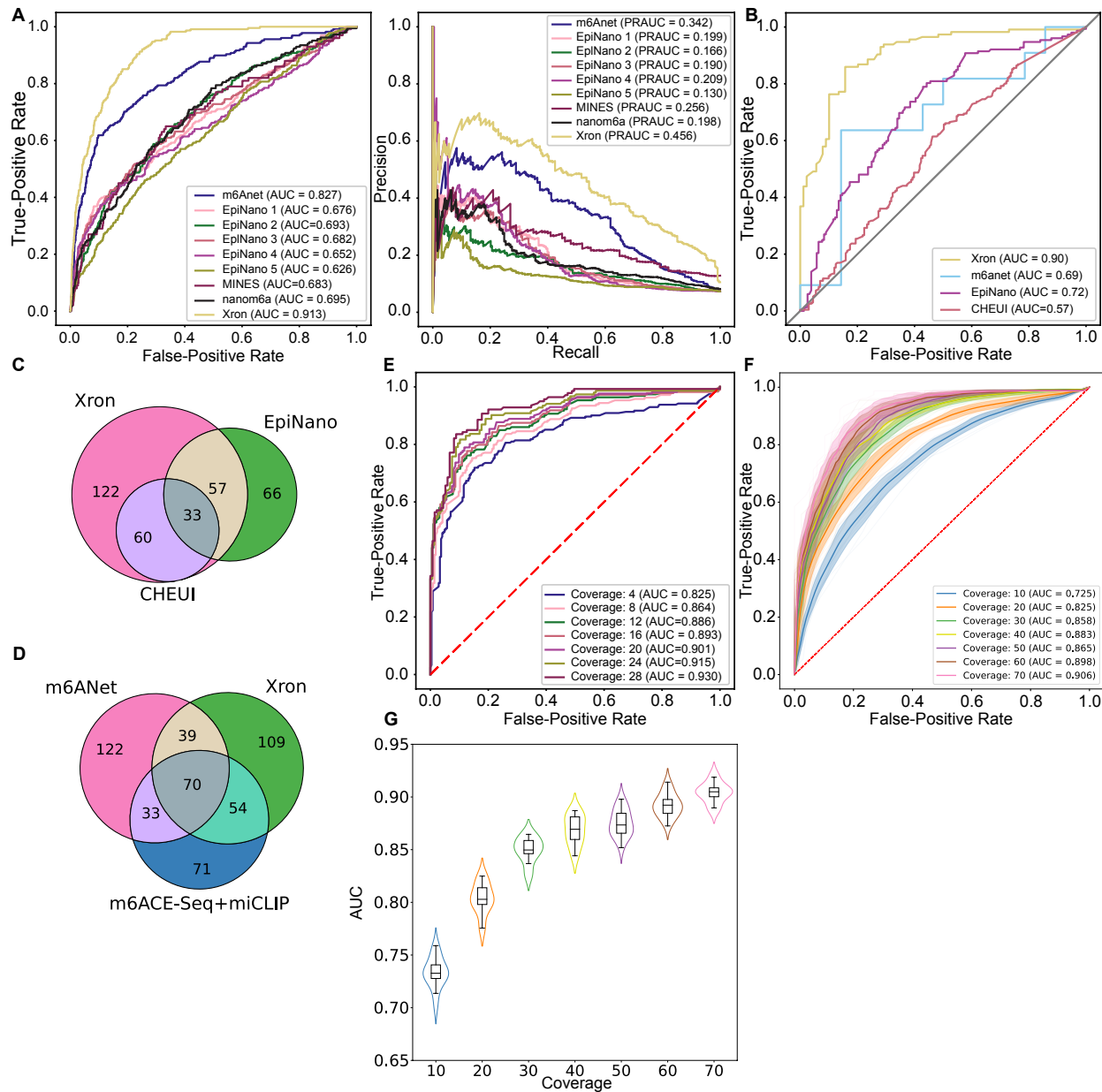


**Fig. 2. Comparison of Xron models across two different species.** (A) ROC and PR curves of m6A prediction on human HEK293T cell line, produced by Xron and other models. (B) ROC curves produced by Xron and other models on yeast data. (C,D) Venn diagram showing the overlapping sites predicted by Xron and other methods on Yeast (C) and HEK293T (D) data. (E) ROC curves produced by Xron for detecting m6A methylation in yeast data under different minimum sequence coverage thresholds. (F) ROC curves generated by Xron for detecting m6A methylation in down-sampled yeast data with different coverage. (G) Distribution of AUC score of Xron on down-sampled yeast data.

162 an Xron model fine-tuned on the human HEK293T cell line on yeast data and obtained similar accuracy  
 163 (Supplementary Fig. S3A).

164 **Xron detects more methylation sites and achieves high accuracy under low coverage settings**

165 As m6Anet intrinsically requires a minimum coverage of at least 20 to obtain site methylation predictions.  
166 This results in a much smaller sample size (11 sites detected). In the same setting, Xron yields 171 sites  
167 with a minimum coverage of 20 on the yeast dataset, which results in higher AUC-ROC accuracy than  
168 m6Anet (0.90 versus 0.69). In total, Xron detects 272 sites reported in the IP data, compared to the 156  
169 sites detected by Epinano and the 93 sites detected by CHEUI (Fig. 2C). Sites detected by Xron also show  
170 higher support from the IP technique (124) compared to m6Anet (107) in the HEK293T cell line (Fig. 2D).  
171 While different methods identify various m6A methylation sites, many sites are detected exclusively by one  
172 method. This observation aligns with previous reports (Koh et al. 2019; Hendra et al. 2022).

173 We next tested if including more low-coverage sites by setting different minimum sequencing coverage  
174 thresholds would influence the prediction accuracy of Xron (Fig. 2E). We found that increasing the read  
175 coverage yielded superior site-level methylation prediction accuracy, increasing from a 0.825 AUC-ROC  
176 score for a minimum read coverage level of 4 to a 0.930 AUC-ROC score with a minimum read coverage  
177 level of 28. This suggests that with higher sequencing depth, Xron can further enhance the precision and  
178 accuracy of methylation detection. Meanwhile, Xron outperforms other models by a large margin even  
179 when setting the minimum read coverage level to 4, with AUC 14% more than the second best model,  
180 Epinano (0.825 versus 0.72). Furthermore, to evaluate Xron's performance in low-coverage regions, we  
181 down-sampled the reads to limit the maximum coverage at each site to a range of 10 to 70. Xron achieved  
182 an accuracy of 0.725 with maximum coverage of 10, outperforming other models with full data (Fig. 2F,G).

183 With the ability of Xron to detect methylation in low-coverage regions or even at the single-read level, we  
184 were able to check the read-level statistics of methylated *k*-mers. A comparison of the read-wise and site-  
185 wise relative frequency of methylated *k*-mers in yeast, human, and *Arabidopsis* shows differences in *k*-mer  
186 profiles across species. Site-wise counting treats multiple reads at one site as a single occurrence, while  
187 read-wise counts *k*-mer occurrence for each read and each site separately (Supplementary Fig. S7A-  
188 E). For yeast, the most frequently used motifs AGACA, GGACA, AGACT, and GGACT from the read-wise  
189 counting are also the most widely used motifs from the site-wise counting. But in human cell lines and  
190 *Arabidopsis*, read-wise counting indicates the most frequently used motif is different than the previously  
191 reported site-wise most "frequently" used motif, which is indicated by the site-wise counting. Motif GAACA in  
192 human cell lines has the highest (>17%) relative frequency in the read-wise count, exceeding the previously  
193 reported most methylated motif GGACT (~12%), but it only possesses <8% relative frequency in the site-

194 wise count while GGACT has >12% relative frequency. Motif TAACT in *Arabidopsis* has the highest ( $\approx$ 15%)  
195 relative frequency in the read-wise count, but drops to <10% in the site-wise count. The variation in  $k$ -mer  
196 profiles across different species offers an ideal scenario for assessing the generalizability of Xron. When  
197 comparing the Xron model finetuned on yeast and human datasets with different  $k$ -mer profiles, we found  
198 they give similar accuracy on yeast, human, and *Arabidopsis* datasets (Fig. 2A,B, Supplementary Fig. S3A-  
199 C).

200 **Xron achieves nearly optimal site-level prediction on a synthesized RNA dataset**

201 We evaluated Xron on a synthesized RNA IVT dataset (Liu et al. 2019) obtained from a different replicate  
202 than the training dataset (see the Methods section). In this dataset, the true methylation modifications were  
203 known for each position in each read, as the reads were either from a fully modified or a fully unmodified  
204 run. Our model achieved an AUC ROC of 0.93 on the single-read-level prediction task (Fig. 3C), in which the  
205 model has to predict m6A bases or A bases for each read at DRACH sites identified by previous antibody  
206 immuno-precipitation experiments (Schwartz et al. 2013). Our model outperforms the second-best read-  
207 level model (m6Anet) by 3% (0.93 versus 0.90) and achieves an almost optimal AUC ROC of >0.99 for  
208 site-level prediction (Fig. 3D), outperforming the second-best site-level model (CHEUI) by nearly 2% ( $\approx$ 1  
209 versus 0.98).

210 **Xron provides m6A stoichiometry**

211 By aligning the reads to the reference genome and piling up the single-read m6A modification predictions  
212 for different sites, Xron can predict site-level m6A modification stoichiometry, i.e., the fraction of modified  
213 bases at a site. We evaluated this ability using a synthetic dataset.

214 The dataset was a mixture created by randomly sampling reads from fully modified or unmodified IVT  
215 datasets (Liu et al. 2019) with specific mixture proportions, which included 0%, 10%, 20%, 30%, 40%,  
216 50%, 60%, 70%, 80%, 90%, and 100%. We calculated the model-predicted m6A proportion as the number  
217 of m6A bases called per site divided by the total number of reads aligned to this site. The median rela-  
218 tive modification proportion followed the same trend as the expected methylation proportion. The trend in  
219 stoichiometry level was successfully recovered (Fig. 3E).

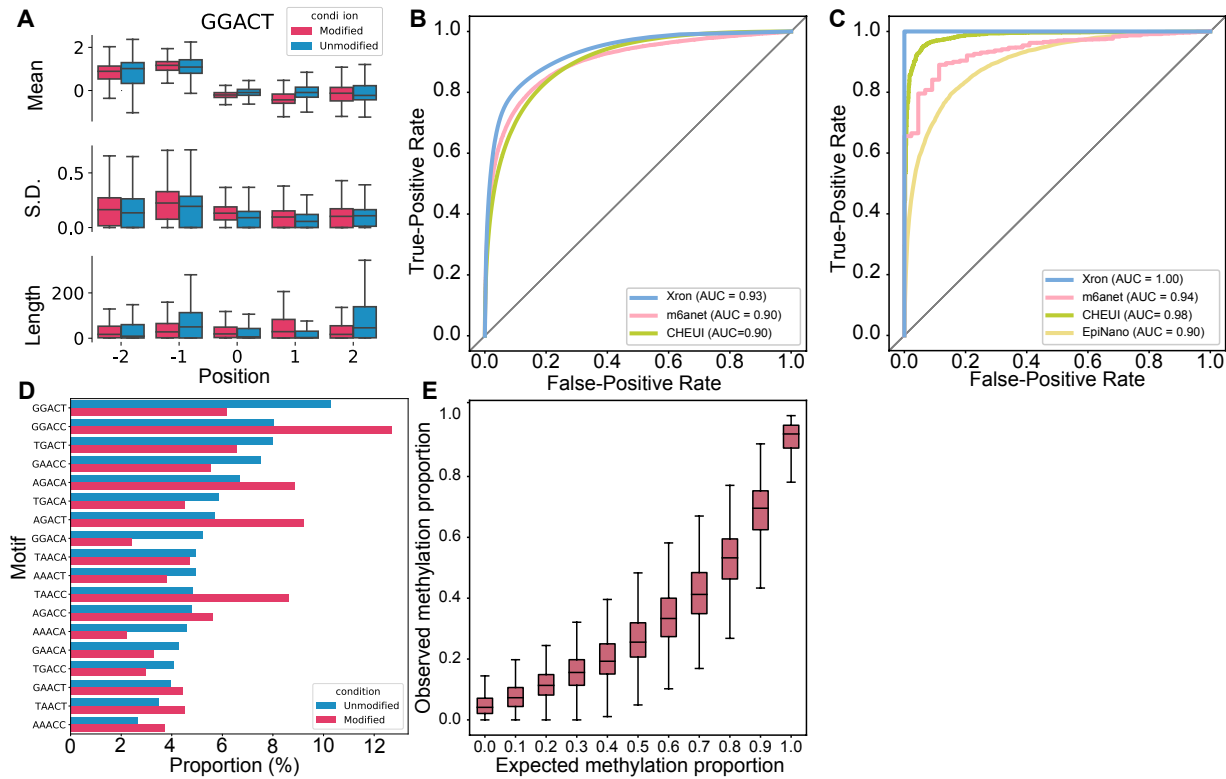


**Fig. 3. Evaluation of the m6A detection results obtained for synthesized IVT RNA reads and stoichiometry prediction.** (A) Box plot comparing the distribution of the mean, standard deviation, and length for the signal segmented by NHMM with 5,232 modified sites and 18,464 unmodified sites for the GGACT motif. Horizontal lines show the median, the box denotes the interquartile range, and the whiskers extend to 1.5 times the interquartile range. Points beyond this range are considered outliers and are removed from the plot. (B,C) ROC curves of Xron against m6Anet and CHEUI for read-level (B) and site-level (C) m6A modification predictions. (D) Bar plot showing the relative proportion of DRACH 5-mer motif for 84,919 modified and 179,717 unmodified positions. (E) Box plot showing the m6A ratio predicted by Xron with different proportions of IVT control and IVT m6A RNA mixing.

## 220 Xron achieved high-accuracy on SQK-RNA004 data

221 We trained an Xron model on a HEK293T cell line dataset from the SG-NEx project, generated using the  
 222 SQK-RNA004 direct RNA sequencing chemistry, a recently released sequencing kit that offers a higher  
 223 sequencing rate and presumably better accuracy. Xron achieved an AUC of 0.91 and a PR-AUC of 0.438  
 224 for all sites (Fig. 4A), and an AUC of 0.92 and a PR-AUC of 0.578 for dense sites (Fig. 4B), surpassing the  
 225 Oxford Nanopore m6A basecaller Dorado and other methods tested on the SQK-RNA002 dataset in the  
 226 same HEK293T cell line. A larger number of detected sites were mutually agreed upon by Xron and Dorado  
 227 and were also supported by immunoprecipitation methods compared to the SQK-RNA002 dataset on the  
 228 same cell line, where most of the sites are detected by only one method (Fig. 4C, Fig. 2C,D). Modified sites

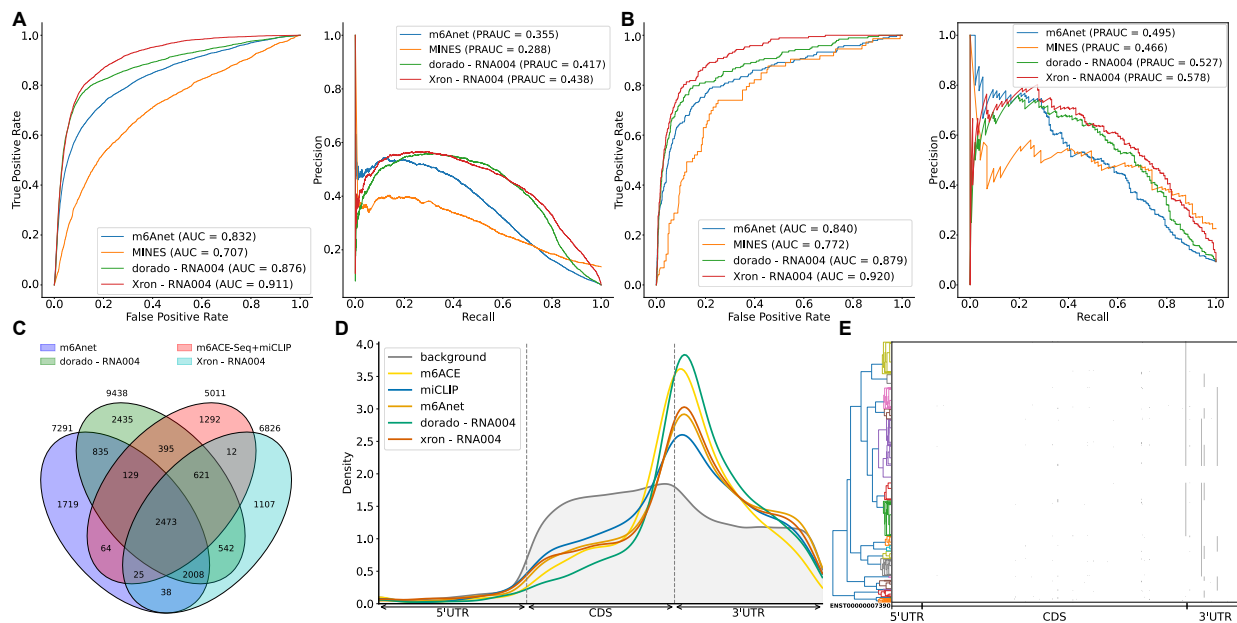


**Fig. 4. m6A detection on SQK-RNA004 dataset.** (A) ROC and PR curve of Xron on SQK-RNA004 data against Dorado. Results of m6Anet and MINES from SQK-RNA002 data on the same HEK293T cell line are also plotted for comparison. (B) Comparison of ROC and PR curves for Xron and Dorado on 2070 dense sites where neighboring modification sites exist within 5 bases. (C) Venn diagram showing the overlapping sites predicted by Xron and other methods on HEK293T cell line. (D) Coordinate distribution of the m6A methylated sites predicted by 5 methods against the background distribution of all DRACH sites. Only sites with at least 20 coverage were chosen. (E) Clustering plot showing the modification of the *TSR3* (ENSG00000007520) mRNA transcript over 780 reads. A modification is called if the predicted probability is greater than 0.9 and is marked with a green dot.

229 detected from SQK-RNA004 data are enriched in the 3' end of the coding sequence along the transcript  
 230 coordinates, as expected for m6A (Fig. 4D).

### 231 Clustering analysis show asynchronous modification

232 Xron enables direct access to read-level modification information, allowing us to examine the modification  
 233 states across multiple sites within each read. Genes that have at least 2 m6A modification sites and with  
 234 at least 500 coverage reads were selected. We found asynchronous modification states around the end of  
 235 CDS and in the 3' UTR region among these reads (Fig. 4E, Supplementary Fig. S8), where m6A methylation  
 236 does not occur synchronously but in a combinatory pattern. For instance, in the *TSR3* gene transcript  
 237 (ENST00000007390.2) at positions 1041, 1096, 1105, and 1151, all 16 possible combinations of modifi-  
 238 cation status at these four sites were observed with varying frequencies. This pattern suggests a complex  
 239 regulatory mechanism based on m6A methylation.

240 **Xron performs consistent basecalling on m6A-modified datasets**

241 To compare the performance of Xron as a basecaller with a canonical basecaller, we evaluated the basecall-  
 242 ing accuracy of Xron and compared it with that of the Guppy ONT basecaller (Table 2 and Supplementary  
 243 Table S2). We evaluated the basecall quality achieved on three datasets: the synthesized IVT RNA dataset,  
 244 the *S. cerevisiae* yeast dataset, and the human HEK293T cell line dataset, considering both modified and  
 245 unmodified reads. When comparing the identity rate, only reads with potential modified sites are taken into  
 246 account. For the synthesized IVT RNA and yeast datasets, we used the second replicate, which was not  
 247 used as training data. Xron suffers less (or no) accuracy drop on datasets with m6A modifications. It exhib-  
 248 ited no performance loss on datasets with methylation compared to the control dataset. On the other hand,  
 249 Guppy showed performance decreases on all three datasets with methylation compared to its performance  
 250 on the unmodified control datasets, including a 14.47% drop in the identity rate on the synthesized reads  
 251 and a 7.55% drop in the identity rate on the HEK293T reads. Guppy also shows a larger context bias for  
 252 *k*-mers from DRACH motifs, comparing to Xron on the HEK293T reads (Supplementary Fig. S6), explaining  
 the identity rate drop on basecalling m6A-modified reads.

**Table 2. Accuracy comparison between Xron and Guppy on three different datasets and their control datasets.**

The identity rate (%) was defined as the number of matched bases in the query sequence divided by the number of bases in the reference sequence (the higher the better). All reported rates are mean values among the aligned reads.

Condition	Model	Identity rate (%) (↑)	Identity rate change (%)
IVT Control	Xron	87.35	—
	Guppy	92.75	—
IVT m6A	Xron	88.48	1.13
	Guppy	78.28	-14.47
Yeast <i>ime4Δ</i> KO	Xron	83.42	—
	Guppy	92.50	—
Yeast	Xron	83.96	0.54
	Guppy	91.94	-0.56
HEK293T <i>METTL3</i> KO	Xron	85.91	—
	Guppy	93.19	—
HEK293T	Xron	87.12	1.21
	Guppy	85.64	-7.55

253

254 **Discussion**

255 Several computational methods (Liu et al. 2019; Jenjaroenpun et al. 2021; Leger et al. 2021; Gao et al.  
 256 2021; Mateos et al. 2022) have been used to detect m6A methylation. These methods require accurate train-

257 ing data, usually obtained using synthesized RNA reads containing the modification of interest, obtained  
258 through experimental methods such as m6ACE-seq or miCLIP, or from a comparative analysis against con-  
259 trol data. However, these methods exhibit a performance drop when they are applied to other datasets,  
260 implying the existence of overfitting. In addition, these methods usually can only provide site-level methy-  
261 lation, losing read-level resolution. We developed an end-to-end m6A modification detection system for  
262 nanopore direct RNA sequencing and were among the first to create a m6A-distinguishing base caller. Our  
263 system, Xron, includes an NHMM model for  $k$ -mer decoding and a neural network basecaller. By employing  
264 data augmentation and semi-supervised learning, we constructed an NHMM that is capable of performing  
265 accurate signal sequence alignment and introduced a novel training dataset for m6A methylation detection.  
266 The training pipeline established in our work facilitates supervised basecaller training without necessitating  
267 complex feature engineering and using both IVT and IP data available to overcome overfitting.

268 Quantifying the transcriptome-wide modification rates is one of the key challenges in methylation detection.  
269 From the read-level methylation states given by Xron, the modification stoichiometry for each site can be  
270 obtained. Meanwhile, our method does not require a high minimum coverage depth, which is essential  
271 for detecting methylation in low-expression regions. Comparative methods detect methylation by analyzing  
272 data from different conditions (Leger et al. 2021; Pratanwanich et al. 2021). While Xron does not require a  
273 control sample to detect methylation, it can facilitate the use of a control sample by comparing the same  
274 site across samples. In addition, compared to other methods where the model performance is influenced  
275 by aspects such as base-calling algorithms, accuracy in the alignment of the reference sequence to signal,  
276 and segmentation of the raw signal, Xron reads out methylation information directly from the raw signal.  
277 More training data on different experimental protocols and different organisms will likely further improve the  
278 accuracy of Xron and other supervised approaches, while the training framework of Xron can easily adopt  
279 these additional training data into the finetuning pipeline.

280 As a basecaller, Xron achieves a consistent identity rate among methylation and unmethylation datasets.  
281 Although there is a performance gap in terms of identity rate between Xron and the basecaller Guppy,  
282 this is likely due to the different neural network architecture used. In future research, it would be bene-  
283 ficial to investigate various neural network structures since previous studies have shown that alterations  
284 to the convolutional-recurrent neural network architecture can yield enhanced basecalling accuracy. For  
285 example, Guppy uses QuartzNet (Kriman et al. 2020), a neural network designed initially for speech recog-

286 nition. SACall (Huang et al. 2020) employs an attention mechanism, while RODAN (Neumann et al. 2022)  
287 integrated squeeze-and-excitation (Hu et al. 2018) layers into a base CNN.

288 Currently, the NHMM takes only raw signal as its input. This has several advantages, including being easy  
289 to train and having a closed-form solution for parameter estimation. However, additional input features can  
290 be added to the NHMM, including the encoded representation from the neural network base caller. The  
291 strategy used by NHMM can also help provide more accurate signal segmentation in other downstream  
292 current-based applications, such as post-basecalled sequence correction (e.g., Nanopolish by Simpson et  
293 al. (2017)). We leave this as future work. Xron was used to detect m6A modification, however, our framework  
294 is suitable for training a basecaller for detecting any natural post-transcription modification, including DNA  
295 methylation such as 5mC and other types of RNA modification. Xron can also be retrained to detect artificial  
296 modifications at a single-molecule level, such as detecting modifications introduced in small non-coding  
297 RNA (Shi et al. 2022).

## 298 Methods

299 Xron is trained using both IVT and IP datasets to obtain better performance. It was first trained on a sur-  
300 rogated IVT dataset and then fine-tuned on IP data. To make efficient finetuning and to avoid overfitting to  
301 the all-or-none methylated reads in IVT data when training with the long current signal, we create partially  
302 methylated reads using data augmentation, first segmenting the signal and then cross-linking the reads  
303 and its corresponding signal in silico. To achieve this, we design a novel nonhomogeneous hidden Markov  
304 model (NHMM) that can be trained to conduct signal segmentation in a semi-supervised fashion on modified  
305 reads, even when lacking methylation labels. The NHMM is trained using the forward-backward algorithm  
306 with its transition matrix conditioned on a canonical basecalled sequence and its alignment, thus giving the  
307 maximum a posteriori estimation of the model parameters regarding methylation base. The Viterbi path of  
308 the NHMM gives the alignment between the current signal and sequence. Following the signal segmentation  
309 process with the NHMM, we prepared a partially methylated dataset through data augmentation, splicing  
310 the fully methylated and unmethylated segments. Training on this augmented dataset diminishes the induc-  
311 tive bias of the model on partially methylated reads when training with entirely methylated or nonmethylated  
312 reads. We then trained an end-to-end methylation-detection basecaller on the augmented dataset, and it  
313 achieved high-accuracy methylation base detection at a single-read resolution. We further improved the  
314 basecaller by applying a fine-tuning procedure on IP data with label smoothing to obtain a more accurate

315 basecalling model. Finally, we benchmarked different m6A detection methods on three datasets, including  
316 a synthetic IVT dataset, a yeast dataset, and a human HEK293T cell line, demonstrating that Xron yields  
317 accurate methylation-aware basecalls and generalizes to different species.

318 **NHMM trained using semisupervised learning**

319 We design a hybrid framework to conduct signal segmentation and alignment when methylated bases are  
320 present. A homogeneous HMM (we refer to this model as an HMM throughout the remainder of this paper  
321 for convenience), as employed in the Nanopolish preprocessing tool (Simpson et al. 2017), faces challenges  
322 when applied to sequences with methylation bases. The absence of ground truth for the methylation states  
323 in each basecalled sequence prevents supervised HMM training. However, training the HMM unsupervised,  
324 using only signal and reference genome, is difficult due to the high noise contained in nanopore sequencing  
325 signals, the long lengths of the electrical signals, and the similar signal levels between certain  $k$ -mers and  
326 their methylated counterparts. Additionally, totally unsupervised training is not necessary as we already  
327 have the canonical basecalled sequence with alignment given by the canonical basecaller and the refer-  
328 ence genome. Although the signals are error-prone in the methylated region, they still provide a general  
329 sketch of the sequence. Thus, instead of performing unsupervised learning with the HMM, we develop a  
330 semi-supervised training process using an NHMM, where we use the basecalled canonical sequence as a  
331 prior when building the transition chain backbone in the NHMM. In contrast with an HMM possessing a ho-  
332 mogeneous transition matrix that remains constant over time  $t$ , an NHMM possesses a nonhomogeneous  
333 transition matrix that depends on the external variables and varies over time  $t$ , allowing the use of dynamic  
334 control for the transition process. Various NHMMs have been used in meteorology (Hughes et al. 1999)  
335 and economics (Netzer et al. 2008; Meligkotsidou & Dellaportas 2011) by constructing transition matrices  
336 that depend on time-varying covariates, such as seasonality (Hughes et al. 1999) or economic cycle indi-  
337 cators (Meligkotsidou & Dellaportas 2011). In our case, the base probabilities along time  $t$  predicted by an  
338 existing canonical basecaller (a base caller trained to predict only canonical bases) are used as the time  
339 covariates of the transition matrix. This approach enables the model to concentrate on the section of the  
340 Markov chain guided by the predicted base probability (Fig. 1C), rather than dealing with the entire chain  
341 as is required in unsupervised learning using HMM, which is more challenging and error-prone.

342 **NHMM for methylated sequence segmentation and alignment**

343 The NHMM represents the input sequence of raw current signals as  $X = (x_1, \dots, x_T)$  for a given  $k$ -mer  
 344 sequence  $Z = (z_1, \dots, z_T)$  inside a nanopore over the sequencing duration  $T$ . Each signal point  $x_t$  repre-  
 345 sents a normalized current value, while  $z_t$  is a variable indicating the  $k$ -mer at time  $t$ . The transition matrix of  
 346 the NHMM is constrained on the basecalled sequence and its alignment given by the canonical basecaller.  
 347 More specifically, suppose we are given the base probability matrix  $H = (h_1, \dots, h_T) \in \mathbb{R}^{B \times T}$ , where  $B$  is  
 348 the number of bases and  $h_t^b$  is the probability of base  $b$  at time  $t$ , which is obtained from an existing canon-  
 349 ical neural network basecaller (Fig. 1A) (Graves et al. 2006; Teng et al. 2018). From the base probability  
 350 matrix  $H$ , we extract the most probable basecalled sequence  $Y = \{y_\tau\}$  and its corresponding alignment  
 351  $A(t)$  which aligns the signal point time  $t$  to sequence index  $\tau$ , giving  $t \rightarrow \tau$ . After correcting the basecalled  
 352 sequence with the reference genome, we construct a reference  $k$ -mer sequence  $C$  by sliding a window of  
 353 size  $k$  (in our case,  $k = 5$ ) across the basecalled sequence, moving one base at a time. Each windowed  
 354 segment forms a  $k$ -mer and is added to the sequence  $C = \{c_\tau\}$ . From now on, to simplify the notation,  
 355 we use  $c_t$  to denote the corresponding  $k$ -mer at time  $t$  after transitioning through alignment  $c_{A(t)}$ . All time  
 356 offsets of the  $k$ -mer sequence reside in the sequence domain, meaning  $c_{t-1}$  refers to  $c_{A(t)-1}$ . Finally, we  
 357 derived the  $k$ -mer transition matrix  $\Psi$  from  $k$ -mer sequence  $C$ ; for details, see the next section. Then, the  
 358 likelihood of observing an electrical signal  $X$  is given by:

$$P(X | C) = \sum_Z \left[ \prod_{t=1}^T P(x_t | z_t) \prod_{t=1}^T P(z_t | z_{t-1}, c_{t-\lfloor m/2 \rfloor}, \dots, c_{t+\lfloor m/2 \rfloor}) \right]. \quad (1)$$

359 Here,  $Z$  is the hidden state representing the underlying  $k$ -mer sequence,  $z_t$  is the  $k$ -mer at time  $t$ , and  
 360  $c_{A(t)}$  is the corrected  $k$ -mer representation at time  $t$  acquired from the canonical neural network output  $H$   
 361 (Fig. 1A).  $T$  is the maximum time stamp for a given sequence segment.  $m$  is the window size for the  $k$ -mers  
 362 to be considered.  $P(x | z)$  is the emission probability of the signal  $x$  given the  $k$ -mer  $z$ , as modeled by a  
 363 Gaussian distribution.

364 **Constructing a transition matrix from the base-called sequence and its alignment**

365 We loosely constrain the transition matrix at time  $t$  in the nonhomogeneous HMM by using the base pre-  
 366 diction output  $H$  derived from a canonical basecaller, thereby using the segmentation results provided by  
 367 the basecaller in an error-tolerant manner (Fig. 1B). By calculating the most probable path from  $H$ , we can  
 368 obtain both the basecalled sequence and the alignment between each base within the most probable path

369 and the sequencing time  $t$ . Following this, we correct the basecalled sequence using the reference genome,  
 370 and we also make appropriate revisions to the alignment to address the deletion or insertion errors in the  
 371 basecalled sequence. We transform the corrected sequence into a  $k$ -mer sequence  $C = \{c_t : t = 1, \dots, T\}$ ,  
 372 incorporating the  $k$  bases surrounding each base in the basecalled sequence; then, this  $k$ -mer sequence is  
 373 reformatted into transition matrices  $\Psi = \{\psi_t : t = 1, \dots, T\}$  by including at most  $m$  transitions, where each  
 374  $\psi_t$  is the temporal transition matrix at time  $t$ . During the process of constructing the  $k$ -mer sequence  $C$  from  
 375  $H$ , the basecalled RNA sequence is corrected by aligning it to a reference genome through the following  
 376 steps:

- 377 – For mismatched bases, we replace the bases in the  $k$ -mer with the reference bases.
- 378 – For insertions/deletions in the base-called sequences that are smaller than five bases, we determine  
 379 the new signal alignment boundary of the inserted/deleted bases by evenly merging/splitting the signal  
 380 boundaries of nearby bases; i.e., we redistribute the occupancy of the inserted bases to the nearby  
 381 bases and allocate occupancy for the deleted bases from the nearby bases.
- 382 – We skip the sequence segments with insertions and deletions that are larger than five bases for quality  
 383 control purposes.

384 The transition matrix  $\Psi$  is then constrained by  $C$ , masking out the irrelevant transition paths so that only  
 385 transition paths that are likely to occur at time  $t$  are retained. To more clearly see what these temporal tran-  
 386 sition matrices stand for, let  $\psi_{i,j}^t = \Pr(z_t = i \mid z_{t-1} = j, c_{t-\lfloor m/2 \rfloor}, \dots, c_{t+\lfloor m/2 \rfloor})$  be the transition probability  
 387 from  $k$ -mer  $i$  to  $k$ -mer  $j$  given constraint  $k$ -mers  $c_i$  from a time window with a width of at most  $m$ , i.e., from  
 388  $t - \lfloor m/2 \rfloor$  to  $t + \lfloor m/2 \rfloor$ . At the start and end of sequence, the window size is less than  $k$  due to boundary  
 389 constraints. In comparison with the transition matrix  $\phi_{i,j} = P(z_t = i \mid z_{t-1} = j)$  of a homogeneous HMM,  
 390 the transition matrix now changes over time  $t$ :

$$\psi_{i,j}^t = \sum_{t'=t-\lfloor m/2 \rfloor}^{t+\lfloor m/2 \rfloor} e_{c_{t'}} \otimes e_{c_{t'+1}} \odot \phi_{i,j}, \quad (2)$$

391 where  $\otimes$  is the tensor product operation,  $\odot$  denotes elementwise multiplication,  $e_i$  is a one-hot vector where  
 392 only the  $i^{th}$  element is 1, and  $\phi_{i,j}$  is the transition matrix in which  $\phi_{i,j} = 1$  if the transition from  $k$ -mer  $i$   
 393 to  $k$ -mer  $j$  is valid (otherwise, it is 0). For example, AACT to AACTA is valid, while AACT to ACTCC is  
 394 not, as we only allow 1 base step.  $\psi_{i,j}^t$  is the  $k$ -mer transition matrix from the  $k$ -mer sequence described

395 above; it is a binary value matrix indicating the  $k$ -mer transition  $i \rightarrow j$  at time  $t$ , where 1 denotes a possible  
 396 transition and 0 represents an impossible transition.

397 We construct the transition matrix from  $m$  nearby  $k$ -mers instead of only the  $k$ -mer at time  $t$  from  $k$ -mer  
 398 sequence  $C$  because the base probability predicted by the canonical basecaller is not exact due to the  
 399 connectionist temporal classification (CTC) loss used (Graves et al. 2006; Teng et al. 2018) and the inser-  
 400 tion/deletion errors in the sequence, nor is it totally correct due to the previously unseen modified bases.  
 401 Thus, we allow the NHMM to explore the alignment space in two ways. First, at each time point, the transition  
 402 matrix of the NHMM is restricted to the current transition probability and the  $m$  nearby transition probabili-  
 403 ties, where  $m$  is a hyperparameter (Eq. 2). This is done to make sure that the final alignment output by the  
 404 NHMM is not too far away from the given the alignment from canonical basecalling but still allows for explo-  
 405 ration within the  $m$ -base window. Second, the transition path of the underlying Markov chain is broadened  
 406 to encompass all possible modified counterparts for each  $k$ -mer along the path (Fig. 1C). As an example,  
 407 AACGT is extended to include four alternative  $k$ -mers with modified bases, AACGT (the original  $k$ -mer),  
 408 AMCGT, MACGT, and MMCGT, leading to expanded paths. After the transition matrix is constructed for all  
 409 the time points, the NHMM is then trained using the expectation-maximization (EM) algorithm (Baum et al.  
 410 1970) until it converges (Fig. S2B).

411 **Preparing the training data with data augmentation and read sampling**

412 All-or-none methylated reads exhibit either complete methylation of all adenine (A) bases or none at all,  
 413 whereas in actual biological samples, methylation typically occurs less frequently and is more sporadically  
 414 distributed. To prevent the neural network from overfitting to all-or-none methylation reads, we create a  
 415 training dataset containing partially methylated reads with labels. This is accomplished by dividing the sig-  
 416 nals from the all-or-none modified reads into smaller segments and subsequently splicing them together.  
 417 The corresponding sequences are recombined according to their alignment with the signal, as provided by  
 418 the NHMM. Merging the signals generated from distinct  $k$ -mers at their junction points can result in sub-  
 419 stantial discrepancies between the combined signal and the actual signal obtained from a real sequencing  
 420 run. To avoid such deviations caused by  $k$ -mer mismatches, we ensure that the preceding and succeeding  
 421  $k$ -mers at the joint sections are identical. For instance, we can merge the signal segments with base-called  
 422 sequences such as GGM**CGTTC**XXX and XXX**CGTTC**TAG to form GGM**CGTTC**TAG. To achieve this, we  
 423 define nonmethylatable  $k$ -mers as  $k$ -mers without adenine (**CGTTC** in the example). They have the same  
 424 sequencing signal distributions in both modified and unmodified reads, making them suitable for use as

425 joint anchors. We employ the trained NHMM to decode both the canonical and fully modified reads in the  
426 training IVT dataset, using the base probability prediction from the canonical basecaller as described be-  
427 fore. The alignment between the sequence and signal is established through a Viterbi path, which assigns  
428 each signal point to its corresponding  $k$ -mer (Fig. 1D). Each read is subsequently divided into segments at  
429 nonmethylatable  $k$ -mers. These segments are used to construct a  $k$ -mer signal graph, where each node  
430 represents an invariant  $k$ -mer. Each edge corresponds to a signal segment whose aligned sequence be-  
431 gins and ends at the respective  $k$ -mers of the connected nodes (Fig. 1E). We then perform a random walk  
432 on the graph, choosing the next edge via an  $\epsilon$ -greedy sampling strategy with an upper confidence bound  
433 (UCB) (Sutton & Barto 2018), as used in the multi-armed bandit algorithm, to ensure maximum diversity in  
434 the sampling sequence (see Algorithm 1 in the supplementary materials).

435 **Data processing**

436 **Acquisition and processing of direct RNA sequencing datasets** All datasets used in this study are  
437 acquired from references Liu et al. (2019), Jenjaroenpun et al. (2021), Workman et al. (2019), Hendra  
438 et al. (2022), and Chen et al. (2021). We obtained both replicates (replicate 1 and 2) from the Epinano  
439 synthesized IVT RNA dataset (Liu et al. 2019) and the only single replicate from the ELIGOS synthe-  
440 sized IVT RNA dataset (Jenjaroenpun et al. 2021). Both of these datasets contain fully modified reads and  
441 unmodified control reads. We also obtained all the NA12878 IVT RNA reads from the Oxford Nanopore  
442 human reference dataset repository: <https://github.com/nanopore-wgs-consortium/NA12878/blob/master/NA12878.RNA.md> (Workman et al. 2019). For the yeast dataset, we obtained all three replicates of the wild strain  
443 and *ime4*-knockout strain (*ime4* $\Delta$ ) (Liu et al. 2019). Reads are extracted if mapped to m6A-modified RRACH  
444 sites previously identified by antibody immunoprecipitation (Schwartz et al. 2013). For the human HEK293T  
445 cell line, we obtained two replicates (replicate 1 and 2) of the wild-type human HEK293T cell (Hendra  
446 et al. 2022) to evaluate models. Following a previous study (Hendra et al. 2022), we used the refer-  
447 ence transcriptome and its genome annotation provided by SG-NEx project: <https://github.com/GoekeLab/sg-nex-data> (Chen et al. 2021). We used the same m6A DRACH sites in the m6Anet paper (Hendra et al.  
448 2022), which were originally identified by m6ACE-seq and miCLIP experiments (Koh et al. 2019; Linder  
449 et al. 2015). We also obtained the first replicate of the wild-type cell line, generated using the SQK-RNA004  
450 sequencing kit from the SG-NEx data repository v5.0.1 (Chen et al. 2021). Currently, there is only one  
451 replicate of this dataset available. Therefore, we split the dataset randomly by reads for training and eval-  
452 uation purposes. For the *Arabidopsis* dataset, we obtained 3 wild-type replicates (Col0-1 to Col0-3) from  
453 454

455 Parker et al. (2020). We used the TAIR10 reference transcriptome (cDNA) and genome from Ensembl:  
456 [https://plants.ensembl.org/Arabidopsis\\_thaliana/Info/Index](https://plants.ensembl.org/Arabidopsis_thaliana/Info/Index). All replicates in the datasets are biological replicates, which are independent biological samples sequenced using the same direct RNA nanopore sequencing protocol. As for synthesized IVT reads, RNA replicates were transcribed from synthesized DNA reads with different sequences. See the sections below for details on replicates used for training and evaluating.

460 All SQK-RNA002 samples were generated using the Nanopore R9.4.1 flow cell, except for the human IVT data, which came from the R9.4 flow cell. The only significant difference between the two flow cells is the 461 slightly improved yield in the R9.4.1. SQK-RNA004 samples were generated using the FLO-PRO004RA flow cell (Chen et al. 2021).

464 The IVT RNA datasets were obtained from Epinano project (Liu et al. 2019) through the GEO database  
465 (GSE124309). The ELIGOS IVT RNA datasets were obtained from ELIGOS project (Jenjaroenpun et al.  
466 2021) through the SRA database (SRP166020). The yeast datasets (wild and *ime4*-knockout) were ob-  
467 tained from Epinano Project (Liu et al. 2019) through the GEO database (GSE126213). The HEK293T cell  
468 lines data were obtained from the SG-NEx Project (Chen et al. 2021) through ENA (PRJEB40872). The  
469 Arabidopsis data were obtained through ENA (PRJEB32782). The SQK-RNA004 data was an early-access  
470 dataset obtained from the SG-NEx data repository v5.0.1.

471 **Canonical basecalling and mapping** All reads in the training dataset were basecalled using the Guppy  
472 5.0.11 ONT basecaller (Oxford Nanopore Technologies 2021) and then mapped to the reference genome  
473 using minimap2 v2.24 (Li 2018) with the settings “-ax map-ont -uf --secondary=no --MD”. The mapped  
474 reads were then transferred to the BAM format using SAMtools 1.11.0 (Li et al. 2009). A canonical neural  
475 network basecaller with the same structure as the CRNN was then trained using the NA12878 IVT reads,  
476 and this basecaller was then used to produce the base probability prediction. This canonical basecaller is  
477 used as a starting model when we retrain it on the augmented IVT data and subsequently fine-tune it on  
478 the yeast data (Liu et al. 2019).

479 **Training datasets** We randomly selected 300,000 canonical (unmodified) read chunks and 300,000 fully-  
480 modified read chunks from replicate 1 of each of the two synthesized IVT RNA datasets (Liu et al. 2019;  
481 Jenjaroenpun et al. 2021), as well as the first 300,000 canonical read chunks from the Oxford Nanopore Hu-  
482 man IVT reference dataset (Workman et al. 2019) to construct the *k*-mer signal graph we described above.  
483 Reads were filtered out if the corresponding basecalled sequence was shorter than three bases, if the signal

484 had a dwell time (the putative duration a  $k$ -mer remains in the pore) exceeding 2000 signal time points, if the  
485 basecalled sequence could not be aligned to the reference genome, or if a single base type comprised more  
486 than 60% of the basecalled sequence. This filtering process resulted in 228,983 canonical read chunks and  
487 204,822 methylated read chunks from the first synthesized IVT dataset (Liu et al. 2019), 195,161 canonical  
488 read chunks and 213,085 methylated read chunks from the second synthesized IVT dataset (Jenjaroenpun  
489 et al. 2021), and 188,004 canonical read chunks from the Human IVT reference dataset (Workman et al.  
490 2019). Methylation sites identified by antibody immunoprecipitation (Schwartz et al. 2013), derived from the  
491 first replicate of the wild-type and the first replicate of the *ime4Δ* from the yeast dataset (Liu et al. 2019)  
492 were used to create the fine-tuning dataset. We regarded all sites from the wild-type strain as methylated  
493 and all sites from the *ime4Δ* strain as unmethylated. However, we considered these classifications noisy  
494 labels and used label smoothing during fine-tuning. Human HEK293T cell dataset (Hendra et al. 2022) was  
495 not used for training and only used in the evaluation.

496 **Evaluation datasets** All the accuracy evaluation datasets we used are sourced from previously published  
497 resources. These include a synthesized IVT dataset (Liu et al. 2019), a yeast dataset (Liu et al. 2019), and a  
498 human HEK293T cell dataset (Hendra et al. 2022). We used the second replicate from both the synthesized  
499 IVT and yeast datasets, as we had already used the first replicate of these two datasets for training and  
500 fine-tuning, and we used the first replicate of the human HEK293T cell dataset as it was not included in  
501 training. A subset of the human HEK293T cell dataset containing 500 genes was randomly sampled from  
502 the original dataset. For the yeast data, we assessed model performance based on the sites identified by  
503 m6A-seq (Schwartz et al. 2013) for the wild-type strain, and the *ime4Δ* strains where no methylation should  
504 be observed. For evaluation on human data, following previous work (Hendra et al. 2022), we regarded the  
505 combined sites identified by m6ACE-seq (Koh et al. 2019) and miCLIP (Linder et al. 2015) as methylated  
506 sites, and other randomly selected sites with the DRACH motif as unmethylated sites.

507 **Training and fine-tuning a m6A methylation-sensitive neural network basecaller**

508 We used the partially modified reads sampled from the signal  $k$ -mer graph to retrain a canonical basecaller.  
509 Before performing retraining on the pre-trained canonical basecaller, we reinitialized the parameters of  
510 the last fully connected hidden layer with random weights but kept the same standard deviation. We then  
511 retrained the model using a smaller learning rate (0.00001) than the usual learning rate (0.001). We fine-  
512 tuned our model on biological samples with m6A sites identified by antibody experiments (Liu et al. 2019),

513 labeling the A base at each modified site as an m6A base for every read (Fig. S2B). Since the bases  
 514 at methylation sites are usually not methylated in every read, this approach would introduce many false-  
 515 positive labels. To address this issue, we applied label-smoothing to the connectionist temporal classification  
 516 (CTC) loss that was used to train the basecaller. A label sequence of length  $L$  was defined as  $S = \{s_i : i =$   
 517  $1, 2, \dots, L\}$ , and each  $s_i$  belonged to the set  $\{A, C, G, T, M\}$ . The base probability logit output  $H \in \mathbb{R}^{T/K \times N}$   
 518 was a  $(T/K)$ -by- $N$  matrix derived from the basecaller's CRNN, where  $K$  is the total number of strides (i.e.,  
 519 the number of steps the convolutional filter moves across the input at each operation), and  $N$  is the number  
 520 of bases used for prediction plus 1 (a blank symbol). The altered CTC loss with label smoothing under a  
 521 strength factor represented by  $\epsilon$  was then defined as:

$$L = \epsilon L_{CTC}(S_{M \rightarrow A}, H) + (1 - \epsilon)L_{CTC}(S, H), \quad (3)$$

522 where M stands for the m6A base,  $L_{CTC}$  is the usual CTC loss, and  $S_{M \rightarrow A}$  is the sequence in which  
 523 every m6A base is replaced with an A base. We set  $\epsilon = 0.1$  empirically for the fine-tuning process, with an  
 524 expectation that the methylation label is correct with probability  $1 - \epsilon$ .

## 525 Software Availability

526 Code is hosted at GitHub repository <https://github.com/haotianteng/xron>. Xron is available under a GNU  
 527 GENERAL PUBLIC LICENSE v3.0. Xron is built with Python 3.8 and PyTorch 1.12, and has been tested on  
 528 PyTorch 1.13 and 2.0.

## 529 Competing Interest

530 C.K. is a co-founder of Ocean Genomics, Inc. H.T. is supported by funding from Oxford Nanopore Tech-  
 531 nologies plc. M.S. is an employee of Oxford Nanopore Technologies plc.

## 532 Acknowledgements

533 This work was supported in part by the US National Science Foundation [DBI-1937540, IIS-2232121], the  
 534 US National Institutes of Health [R01HG012470], and by the generosity of Eric and Wendy Schmidt by  
 535 recommendation of the Schmidt Futures program. We also thank the Pittsburgh Supercomputing Center for  
 536 providing computational resources through the Bridges2 system. H.T. is supported by funding from Oxford

537 Nanopore Technologies plc and the School of Computer Science, Carnegie Mellon University - The Joint  
 538 CMU-Pitt Ph.D. Program in Computational Biology (CPCB). H.T., Z.B.-J., and C.K. conceived the study.  
 539 H.T. and C.K. designed the Xron algorithm. H.T. implemented the Xron algorithm. H.T. ran the performed  
 540 comparison and analysis. H.T. and M.S. prepared the training data. H.T., Z.B.-J., and C.K. wrote the initial  
 541 draft. H.T., Z.B.-J., M.S., and C.K. refined the manuscript. We used ChatGPT to correct grammatical errors  
 542 and improve the flow of early drafts of this manuscript. We thank Minh Hoang for reviewing the manuscript  
 543 and offering valuable feedback. We thank Tim Massingham (XGenomes Corp.) for the helpful discussion  
 544 on signal segmentation.

545 **References**

546 Abebe JS, Price AM, Hayer KE, Mohr I, Weitzman MD, Wilson AC & Depledge DP. 2022. DRUMMER—  
 547 Rapid Detection of RNA Modifications through Comparative Nanopore Sequencing. *Bioinformatics* **38**:  
 548 3113–3115. doi: [10.1093/bioinformatics/btac274](https://doi.org/10.1093/bioinformatics/btac274)

549 Amores J. 2013. Multiple Instance Classification: Review, Taxonomy and Comparative Study. *Artif Intell*  
 550 **201**: 81–105. doi: [10.1016/j.artint.2013.06.003](https://doi.org/10.1016/j.artint.2013.06.003)

551 Boulias K & Greer EL. 2023. Biological Roles of Adenine Methylation in RNA. *Nat Rev Genet* **24**: 143–160.  
 552 doi: [10.1038/s41576-022-00534-0](https://doi.org/10.1038/s41576-022-00534-0)

553 Buermans H & Den Dunnen J. 2014. Next Generation Sequencing Technology: Advances and Applications.  
 554 *Biochim Biophys Acta, Mol Basis Dis* **1842**: 1932–1941. doi: [10.1016/j.bbadi.2014.06.015](https://doi.org/10.1016/j.bbadi.2014.06.015)

555 Carlile TM, Rojas-Duran MF, Zinshteyn B, Shin H, Bartoli KM & Gilbert WV. 2014. Pseudouridine Profiling  
 556 Reveals Regulated mRNA Pseudouridylation in Yeast and Human Cells. *Nature* **515**: 143–146. doi:  
 557 [10.1038/nature13802](https://doi.org/10.1038/nature13802)

558 Chen K, Lu Z, Wang X, Fu Y, Luo G.-Z, Liu N, Han D, Dominissini D, Dai Q, Pan T, et al. 2015. High-  
 559 Resolution N6-methyladenosine (m6A) Map Using Photo-Crosslinking-Assisted m6A Sequencing. *Angew  
 560 Chem* **127**: 1607–1610. doi: [10.1002/ange.201410647](https://doi.org/10.1002/ange.201410647)

561 Chen Y, Davidson NM, Wan YK, Patel H, Yao F, Low HM, Hendra C, Watten L, Sim A, Sawyer C, et al.  
 562 2021. A Systematic Benchmark of Nanopore Long Read RNA Sequencing for Transcript Level Analysis  
 563 in Human Cell Lines. *bioRxiv* doi: [10.1101/2021.04.21.440736](https://doi.org/10.1101/2021.04.21.440736)

564 D'Aquila P, Montesanto A, Mandalà M, Garasto S, Mari V, Corsonello A, Bellizzi D & Passarino G. 2017.  
 565 Methylation of the Ribosomal RNA Gene Promoter Is Associated with Aging and Age-Related Decline.  
 566 *Aging Cell* **16**: 966–975. doi: [10.1111/acel.12603](https://doi.org/10.1111/acel.12603)

567 Dierks D, Garcia-Campos MA, Uzonyi A, Safra M, Edelheit S, Rossi A, Sideri T, Varier RA, Brandis A,  
568 Stelzer Y, et al. 2021. Multiplexed Profiling Facilitates Robust m6A Quantification at Site, Gene and  
569 Sample Resolution. *Nat Methods* **18**: 1060–1067. doi: 10.1038/s41592-021-01242-z

570 Dominissini D, Moshitch-Moshkovitz S, Schwartz S, Salmon-Divon M, Ungar L, Osenberg S, Cesarkas  
571 K, Jacob-Hirsch J, Amariglio N, Kupiec M, et al. 2012. Topology of the Human and Mouse m6A RNA  
572 Methylomes Revealed by m6A-seq. *Nature* **485**: 201–206. doi: 10.1038/nature11112

573 Fu Y, Dominissini D, Rechavi G & He C. 2014. Gene Expression Regulation Mediated through Reversible  
574 m6A RNA Methylation. *Nat Rev Genet* **15**: 293–306. doi: 10.1038/nrg3724

575 Gao Y, Liu X, Wu B, Wang H, Xi F, Kohnen MV, Reddy AS & Gu L. 2021. Quantitative Profiling of N 6-  
576 Methyladenosine at Single-Base Resolution in Stem-Differentiating Xylem of *Populus Trichocarpa* Using  
577 Nanopore Direct RNA Sequencing. *Genome Biol* **22**: 1–17. doi: 10.1186/s13059-020-02241-7

578 Garalde DR, Snell EA, Jachimowicz D, Sipos B, Lloyd JH, Bruce M, Pantic N, Admassu T, James P,  
579 Warland A, et al. 2018. Highly Parallel Direct RNA Sequencing on an Array of Nanopores. *Nat Methods*  
580 **15**: 201–206. doi: 10.1038/nmeth.4577

581 Garcia-Campos MA, Edelheit S, Toth U, Safra M, Shachar R, Viukov S, Winkler R, Nir R, Lasman L, Brandis  
582 A, et al. 2019. Deciphering the “m6A Code” via Antibody-Independent Quantitative Profiling. *Cell* **178**:  
583 731–747. doi: 10.1016/j.cell.2019.06.013

584 Helm M, Lyko F & Motorin Y. 2019. Limited Antibody Specificity Compromises Epitranscriptomic Analyses.  
585 *Nat Commun* **10**: 5669. doi: 10.1038/s41467-019-13684-3

586 Hendra C, Pratanwanich PN, Wan YK, Goh WSS, Thiery A & Göke J. 2022. Detection of m6A from Direct  
587 RNA Sequencing Using a Multiple Instance Learning Framework. *Nat Methods* **19**: 1590–1598. doi:  
588 10.1038/s41592-022-01666-1

589 Hu J, Shen L & Sun G (2018). “Squeeze-and-Excitation Networks”. In: *Proceedings of the IEEE Conference  
590 on Computer Vision and Pattern Recognition*, 7132–7141. doi: 10.48550/arxiv.1709.01507.

591 Hu L, Liu S, Peng Y, Ge R, Su R, Senevirathne C, Harada BT, Dai Q, Wei J, Zhang L, et al. 2022. m6A  
592 RNA Modifications Are Measured at Single-Base Resolution across the Mammalian Transcriptome. *Nat  
593 Biotechnol* **40**: 1210–1219. doi: 10.1038/s41587-022-01243-z

594 Huang N, Nie F, Ni P, Luo F & Wang J. 2020. Sacall: A Neural Network Basecaller for Oxford Nanopore  
595 Sequencing Data Based on Self-Attention Mechanism. *IEEE/ACM Trans Comput Biol Bioinf* **19**: 614–  
596 623. doi: 10.1109/TCBB.2020.3039244

597 Jenjaroenpun P, Wongsurawat T, Wadley TD, Wassenaar TM, Liu J, Dai Q, Wanchai V, Akel NS, Jamshidi-  
598 Parsian A, Franco AT, et al. 2021. Decoding the Epitranscriptional Landscape from Native RNA Se-  
599 quences. *Nucleic Acids Res* **49**: e7–e7. doi: 10.1093/nar/gkaa620

600 Ke S, Alemu EA, Mertens C, Gantman EC, Fak JJ, Mele A, Haripal B, Zucker-Scharff I, Moore MJ, Park  
601 CY, et al. 2015. A Majority of m6A Residues Are in the Last Exons, Allowing the Potential for 3' UTR  
602 Regulation. *Genes Dev* **29**: 2037–2053. doi: 10.1101/gad.269415.115

603 Ke S, Pandya-Jones A, Saito Y, Fak JJ, Vågbø CB, Geula S, Hanna JH, Black DL, Darnell JE & Darnell RB.  
604 2017. m6A mRNA Modifications Are Deposited in Nascent Pre-mRNA and Are Not Required for Splicing  
605 but Do Specify Cytoplasmic Turnover. *Genes Dev* **31**: 990–1006. doi: 10.1101/gad.301036.117

606 Khoddami V, Yerra A, Mosbruger TL, Fleming AM, Burrows CJ & Cairns BR. 2019. Transcriptome-Wide  
607 Profiling of Multiple RNA Modifications Simultaneously at Single-Base Resolution. *PNAS* **116**: 6784–  
608 6789. doi: 10.1073/pnas.1817334116

609 Koh CW, Goh YT & Goh WS. 2019. Atlas of Quantitative Single-Base-Resolution N6-methyl-adenine Methy-  
610 lomes. *Nat Commun* **10**: 1–15. doi: 10.1038/s41467-019-13561-z

611 Kriman S, Beliaev S, Ginsburg B, Huang J, Kuchai O, Lavrukhin V, Leary R, Li J & Zhang Y (2020).  
612 “Quartznet: Deep Automatic Speech Recognition with 1d Time-Channel Separable Convolutions”. In:  
613 *2020 IEEE International Conference on Acoustics, Speech and Signal Processing (ICASSP)*. IEEE,  
614 6124–6128. doi: 10.48550/arxiv.1910.10261.

615 Leger A, Amaral PP, Pandolfini L, Capitanchik C, Capraro F, Miano V, Migliori V, Toolan-Kerr P, Sideri T,  
616 Enright AJ, et al. 2021. RNA Modifications Detection by Comparative Nanopore Direct RNA Sequencing.  
617 *Nat Commun* **12**: 1–17. doi: 10.1038/s41467-021-27393-3

618 Li H, Handsaker B, Wysoker A, Fennell T, Ruan J, Homer N, Marth G, Abecasis G, Durbin R & 1000  
619 Genome Project Data Processing Subgroup. 2009. The Sequence Alignment/Map Format and SAM-  
620 tools. *Bioinformatics* **25**: 2078–2079. doi: 10.1093/bioinformatics/btp352

621 Linder B, Grozhik AV, Olarerin-George AO, Meydan C, Mason CE & Jaffrey SR. 2015. Single-Nucleotide-  
622 Resolution Mapping of m6A and m6Am throughout the Transcriptome. *Nat Methods* **12**: 767–772. doi:  
623 10.1038/nmeth.3453

624 Liu H, Begik O, Lucas MC, Ramirez JM, Mason CE, Wiener D, Schwartz S, Mattick JS, Smith MA & Novoa  
625 EM. 2019. Accurate Detection of m6A RNA Modifications in Native RNA Sequences. *Nat Commun* **10**:  
626 1–9. doi: 10.1038/s41467-019-11713-9

627 Marchand V, Ayadi L, Ernst FG, Hertler J, Bourguignon-Igel V, Galvanin A, Kotter A, Helm M, Lafontaine DL  
628 & Motorin Y. 2018. AlkAniline-Seq: Profiling of m7G and m3C RNA Modifications at Single Nucleotide  
629 Resolution. *Angew Chem Int Ed* **57**: 16785–16790. doi: 10.1002/anie.201810946

630 Mateos PA, Sethi AJ, Guarnacci M, Ravindran A, Srivastava A, Xu J, Woodward K, Hamilton W, Gao J,  
631 Starrs LM, et al. 2022. Identification of m6A and m5C RNA Modifications at Single-Molecule Resolution  
632 from Nanopore Sequencing. *bioRxiv* doi: 10.1101/2022.03.14.484124

633 McIntyre AB, Gokhale NS, Cerchietti L, Jaffrey SR, Horner SM & Mason CE. 2020. Limits in the Detection  
634 of m6A Changes Using MeRIP/m6A-seq. *Sci Rep* **10**: 6590. doi: 10.1038/s41598-020-63355-3

635 Meyer KD. 2019. DART-seq: An Antibody-Free Method for Global m6A Detection. *Nat Methods* **16**: 1275–  
636 1280. doi: 10.1038/s41592-019-0570-0

637 Meyer KD, Saletoye Y, Zumbo P, Elemento O, Mason CE & Jaffrey SR. 2012. Comprehensive Analysis of  
638 mRNA Methylation Reveals Enrichment in 3' UTRs and near Stop Codons. *Cell* **149**: 1635–1646. doi:  
639 10.1016/j.cell.2012.05.003

640 Molinie B, Wang J, Lim KS, Hillebrand R, Lu Z.-x, Van Wittenberghe N, Howard BD, Daneshvar K, Mullen  
641 AC, Dedon P, et al. 2016. m6A-LAIC-seq Reveals the Census and Complexity of the m6A Epitranscrip-  
642 tome. *Nat Methods* **13**: 692–698. doi: 10.1038/nmeth.3898

643 Murakami S & Jaffrey SR. 2022. Hidden Codes in mRNA: Control of Gene Expression by m6A. *Mol Cell*  
644 **82**: 2236–2251. doi: 10.1016/j.molcel.2022.05.029

645 Neumann D, Reddy AS & Ben-Hur A. 2022. RODAN: A Fully Convolutional Architecture for Basecalling  
646 Nanopore RNA Sequencing Data. *BMC Bioinf* **23**: 1–9. doi: 10.1186/s12859-022-04686-y

647 Parker MT, Knop K, Sherwood AV, Schurch NJ, Mackinnon K, Gould PD, Hall AJ, Barton GJ & Simpson  
648 GG. 2020. Nanopore Direct RNA Sequencing Maps the Complexity of Arabidopsis mRNA Processing  
649 and m6A Modification. *eLife* **9**: e49658. doi: 10.7554/eLife.49658

650 Pratanwanich PN, Yao F, Chen Y, Koh CW, Wan YK, Hendra C, Poon P, Goh YT, Yap PM, Chooi JY, et al.  
651 2021. Identification of Differential RNA Modifications from Nanopore Direct RNA Sequencing with xPore.  
652 *Nat Biotechnol* **39**: 1394–1402. doi: 10.1038/s41587-021-00949-w

653 Qin Y, Li L, Luo E, Hou J, Yan G, Wang D, Qiao Y & Tang C. 2020. Role of m6A RNA Methylation in  
654 Cardiovascular Disease. *Int J Mol Med* **46**: 1958–1972. doi: 10.3892/ijmm.2020.4746

655 Ryvkin P, Leung YY, Silverman IM, Childress M, Valladares O, Dragomir I, Gregory BD & Wang L.-S. 2013.  
656 HAMR: High-Throughput Annotation of Modified Ribonucleotides. *RNA* **19**: 1684–1692. doi: 10.1261/  
657 rna.036806.112

658 Schwartz S, Agarwala SD, Mumbach MR, Jovanovic M, Mertins P, Shishkin A, Tabach Y, Mikkelsen TS,  
659 Satija R, Ruvkun G, et al. 2013. High-Resolution Mapping Reveals a Conserved, Widespread, Dynamic  
660 mRNA Methylation Program in Yeast Meiosis. *Cell* **155**: 1409–1421. doi: 10.1016/j.cell.2013.10.047

661 Shi J, Zhou T & Chen Q. 2022. Exploring the Expanding Universe of Small RNAs. *Nat Cell Biol* **24**: 415–  
662 423. doi: 10.1038/s41556-022-00880-5

663 Sun T, Wu R & Ming L. 2019. The Role of m6A RNA Methylation in Cancer. *Biomed Pharmacother* **112**:  
664 108613. doi: 10.1016/j.biopha.2019.108613

665 Wan YK, Hendra C, Pratanwanich PN & Göke J. 2022. Beyond Sequencing: Machine Learning Algorithms  
666 Extract Biology Hidden in Nanopore Signal Data. *Trends Genet* **38**: 246–257. doi: 10.1016/j.tig.2021.  
667 09.001

668 Zhang Z, Chen L.-Q, Zhao Y.-L, Yang C.-G, Roundtree IA, Zhang Z, Ren J, Xie W, He C & Luo G.-Z.  
669 2019. Single-Base Mapping of m6A by an Antibody-Independent Method. *Sci Adv* **5**: eaax0250. doi:  
670 10.1126/sciadv.aax0250

671 Zhang Z, Chen T, Chen H.-X, Xie Y.-Y, Chen L.-Q, Zhao Y.-L, Liu B.-D, Jin L, Zhang W, Liu C, et al. 2021.  
672 Systematic Calibration of Epitranscriptomic Maps Using a Synthetic Modification-Free RNA Library. *Nat  
673 Methods* **18**: 1213–1222. doi: 10.1038/s41592-021-01280-7

674 Zhong Z.-D, Xie Y.-Y, Chen H.-X, Lan Y.-L, Liu X.-H, Ji J.-Y, Wu F, Jin L, Chen J, Mak DW, et al. 2023.  
675 Systematic Comparison of Tools Used for m6A Mapping from Nanopore Direct RNA Sequencing. *Nat  
676 Commun* **14**: 1906. doi: 10.1038/s41467-023-37596-5



## Detecting m6A RNA modification from nanopore sequencing using a semi-supervised learning framework

Haotian Teng, Marcus Stoiber, Ziv Bar-Joseph, et al.

Genome Res. published online October 15, 2024

Access the most recent version at doi:[10.1101/gr.278960.124](https://doi.org/10.1101/gr.278960.124)

---

**Supplemental Material** <http://genome.cshlp.org/content/suppl/2024/11/04/gr.278960.124.DC1>

**P<P** Published online October 15, 2024 in advance of the print journal.

**Accepted Manuscript** Peer-reviewed and accepted for publication but not copyedited or typeset; accepted manuscript is likely to differ from the final, published version.

**Open Access** Freely available online through the *Genome Research* Open Access option.

**Creative Commons License** This manuscript is Open Access. This article, published in *Genome Research*, is available under a Creative Commons License (Attribution-NonCommercial 4.0 International license), as described at <http://creativecommons.org/licenses/by-nc/4.0/>.

**Email Alerting Service** Receive free email alerts when new articles cite this article - sign up in the box at the top right corner of the article or [click here](#).

---



---

To subscribe to *Genome Research* go to:  
<https://genome.cshlp.org/subscriptions>